Neuron
Article

Electrical Coupling Mediates Tunable Low-Frequency Oscillations and Resonance in the Cerebellar Golgi Cell Network

Guillaume P. Dugué,[1] Nicolas Brunel,[2] Vincent Hakim,[3] Eric Schwartz,[1] Mireille Chat,[4] Maxime Lévesque,[5] Richard Courtemanche,[5] Clément Léna,[1] and Stéphane Dieudonné[1,*]
[1]Laboratoire de Neurobiologie, ENS, CNRS, Paris
[2]Laboratoire de Neurophysique et Physiologie, Université René Descartes, CNRS, Paris
[3]Laboratoire de Physique Statistique, ENS, CNRS, Paris
[4]Laboratoire de Physiologie Cérébrale, Université René Descartes, CNRS, Paris
[5]Department of Exercise Science, Center for Studies in Behavioral Neurobiology, Concordia University, Montréal, Canada
*Correspondence: dieudon@biologie.ens.fr
DOI 10.1016/j.neuron.2008.11.028

SUMMARY

Tonic motor control involves oscillatory synchronization of activity at low frequency (5–30 Hz) throughout the sensorimotor system, including cerebellar areas. We investigated the mechanisms underpinning cerebellar oscillations. We found that Golgi interneurons, which gate information transfer in the cerebellar cortex input layer, are extensively coupled through electrical synapses. When depolarized in vitro, these neurons displayed low-frequency oscillatory synchronization, imposing rhythmic inhibition onto granule cells. Combining experiments and modeling, we show that electrical transmission of the spike afterhyperpolarization is the essential component for oscillatory population synchronization. Rhythmic firing arises in spite of strong heterogeneities, is frequency tuned by the mean excitatory input to Golgi cells, and displays pronounced resonance when the modeled network is driven by oscillating inputs. In vivo, unitary Golgi cell activity was found to synchronize with low-frequency LFP oscillations occurring during quiet waking. These results suggest a major role for Golgi cells in coordinating cerebellar sensorimotor integration during oscillatory interactions.

INTRODUCTION

In the CNS, oscillations provide a temporal framework for the coordination of neuronal assemblies (Gray, 1994; Salinas and Sejnowski, 2001; Schnitzler and Gross, 2005; Sejnowski and Paulsen, 2006; Singer, 1999; Varela et al., 2001). During slow movements and tonic contractions, motor commands are elaborated and conveyed in the form of oscillatory patterns of activity at low frequencies (5–30 Hz), resulting in prominent corticomuscular coherence (Salenius and Hari, 2003). Recent studies have shown that this activity emerges from a large web of oscillatory interactions between sensorimotor areas, including the cerebellum (Schnitzler and Gross, 2005). Low-frequency oscillations are thought to increase the robustness and gain of motor control (Baker et al., 1999) but can also lead to pathological tremors (Salenius and Hari, 2003; Schnitzler and Gross, 2005).

The cerebellum has been specifically associated with the coordination, optimization, and correction of ongoing movements (Mauk et al., 2000). Lesions of the cerebellum are known to cause resting and movement tremors that may be associated with unbalanced oscillatory motor control (Deuschl and Bergman, 2002; Schnitzler and Gross, 2005). Local field potential (LFP) oscillations in the 5–30 Hz range have been recorded in hemispheric regions of the cerebellar cortex of both rats and monkeys (Hartmann and Bower, 1998; Pellerin and Lamarre, 1997). These oscillations are often phase locked with LFP oscillations recorded from the sensorimotor cortex (Courtemanche and Lamarre, 2005; O'Connor et al., 2002). In monkeys, synchronized cerebral and cerebellar oscillations are reproducibly observed in conjunction with steady holding during a sensory-cued lever press task (Courtemanche and Lamarre, 2005; Courtemanche et al., 2002; Pellerin and Lamarre, 1997). Cerebro-cerebellar coherence seems to involve also the deep cerebellar nuclei (DCN), the main cerebellar output centers, since DCN neurons tend to discharge in phase with cortical oscillations during a precision grip task (Soteropoulos and Baker, 2006). In the cerebellar cortex, LFP oscillations appear to be generated at the level of the granular layer (Hartmann and Bower, 1998; Pellerin and Lamarre, 1997). They are accompanied by phase-locked bursts of multiunit activity (Courtemanche et al., 2002; Hartmann and Bower, 1998), probably representing granule cell firing, and appear to constrain the discharge of overlying Purkinje cells (Courtemanche et al., 2002). Although these oscillations can potentially have a great impact on granular layer processing, their origin and properties are still unknown.

In the granular layer, Golgi interneurons are the only source of inhibition for granule cells and are traditionally thought to control the gain of the mossy fiber-granule cell relay (Albus, 1971; Marr, 1969). Since Golgi cells provide a highly divergent output onto

granule cells (Palkovits et al., 1971), they have also been regarded as key elements for the generation of temporal patterns in the cerebellar cortex (De Schutter and Bjaalie, 2001; De Schutter et al., 2000; Forti et al., 2006; Isope et al., 2002; Kistler and De Zeeuw, 2003; Kistler et al., 2000; Maex and De Schutter, 1998). Golgi cells have been considered so far as independent units, but recent evidence that they express gap-junction-forming proteins (Belluardo et al., 2000; Condorelli et al., 2000; Ray et al., 2005, 2006; Vogt et al., 2005; Zappala et al., 2006) suggests that they may interact through electrical synapses. The presence of these putative electrical synapses has not been tested yet, and their influence on the temporal organization of Golgi cells activity remains unknown.

Here, we show that Golgi cells are strongly electrically coupled and display low-frequency oscillatory synchronization upon pharmacological stimulation. Using both paired recordings and network simulations, we found that oscillations in the Golgi cell network critically depend on the transmission of the spike afterhyperpolarization through electrical synapses and do not require any subthreshold resonance mechanisms. This rhythmogenic mechanism allows the Golgi cell population activity to become resonant with oscillatory inputs. Golgi cell coordinated firing translates into rhythmic inhibition and disinhibition of the granule cell population. As expected from our model, Golgi cells recorded in vivo discharged in synchrony with LFP oscillations occurring during quiet wakefulness.

RESULTS

Electrical Coupling between Golgi Cells

Experiments were carried out on cerebellar slices prepared from 20- to 60-day-old GlyT2-eGFP mice (Zeilhofer et al., 2005). Paired recording were performed on GFP-positive Golgi cells, which represent 80% of the overall Golgi cell population (Simat et al., 2007). In 41 out of 45 pairs, the injection of hyperpolarizing current steps into either cell elicited a hyperpolarization of the other (Figure 1B), revealing the existence of electrical coupling. This manipulation returned two values for the junctional conductance (G_J; Experimental Procedures) that were linearly correlated (Figure 1C), showing that the coupling was symmetrical. In 43 pairs, G_J, taken as the average of these two values, was plotted as a function of the intercellular distance (ID; Supplemental Data) (Figure 1D). G_J averaged 0.73 ± 0.41 nS (ranging 0.20–1.99 nS, n = 36) within 0–100 μm and dropped to 0.11 ± 0.10 nS (0.02–0.33 nS, n = 7) above 100 μm (120–215 μm). The coupling coefficient (Experimental Procedures) was larger than 2% for IDs lesser than 100 μm (mean = 8.9% ± 5.1%, ranging 2.5%–22.6%, n = 36). In addition, carbenoxolone (100 μM) reduced G_J by 82.0% ± 8.7%, (n = 4; Figure S2A), indicating that the electrical coupling was due to gap junctions (Davidson et al., 1986). The characteristics of electrical synapses shown here are similar to the ones measured in other interneuronal networks (Blatow et al., 2003; Galarreta et al., 2004; Galarreta and Hestrin, 1999; Gibson et al., 1999; Mann-Metzer and Yarom, 1999).

The existence of chemical synapses between Golgi cells was tested in a subset of electrically coupled pairs (n = 7), in which the internal chloride concentration was elevated ($[Cl^-]$ = 30 mM, E_{Cl-} = −39 mV). One cell was clamped at −75 mV while spikes were triggered in the other cell. To unmask an inhibitory chemical connection, the spikelet evoked in the presence of SR 95531

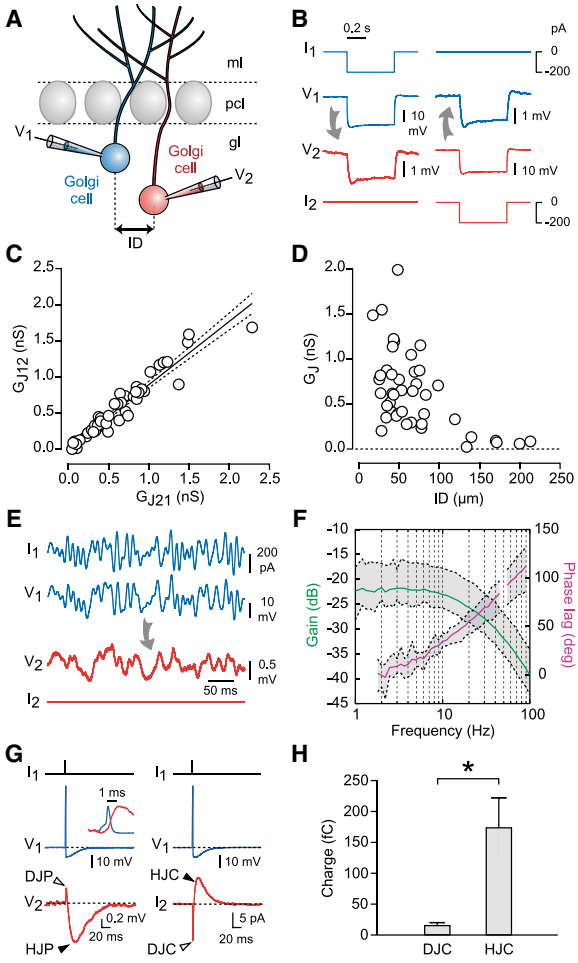

Figure 1. Electrical Synapses between Golgi Cells

(A) Recording configuration. ml, molecular layer; pcl, Purkinje cell layer; gl, granular layer; ID, intercellular distance.

(B) Response of an electrically coupled pair (blue, cell 1; red, cell 2) to hyperpolarizing current steps (−200 pA, 500 ms) injected into cell 1 (left) or cell 2 (right) (averages of 20 sweeps).

(C) The two values of the junctional conductance (G_{J12} and G_{J21}, Experimental Procedures) obtained in each pair (n = 37), plotted against each other. Black line: linear fit (coefficient = 0.88 ± 0.04). Dashed lines: 5%–95% confidence bands.

(D) Junctional conductance (G_J) plotted against the ID (n = 34 pairs).

(E) Response of an electrically coupled pair to injection into cell 1 (blue) of a current waveform with defined spectral content (averages of five sweeps).

(F) Bode plot showing the average frequency response of six connected pairs. The corner frequency (taken at −3 dB below steady-state attenuation) was 17 Hz. Dashed lines: 10th and 90th percentiles.

(G) Spike transmission in coupled pairs. Spikes were triggered in cell 1 (blue) with brief pulses (800 pA, 1 ms, black). The spikelet evoked in cell 2 (red) is shown in current-clamp (left, average of 10 sweeps) and voltage-clamp (right, V_{hold} = −75 mV, average of 390 sweeps). DJP (DJC), depolarizing junctional potential (current); HJP (HJC), hyperpolarizing junctional potential (current). (Inset) Normalized average spike and DJP, showing that the DJP peaks around 1 ms after the spike.

(H) Average amount of charges (±2 SEM) carried by the DJC and the HJC at −75 mV. *$p < 10^{-3}$ (sign test).

(5 μM) and strychnine (600 nM) was subtracted from the control spikelet. No inward current below 2 baseline SD was revealed after the subtraction (Figure S3), indicating that chemical coupling, if any, is not a prominent feature of the Golgi cell network.

Frequency-Dependent Properties of Electrical Synapses between Golgi Cells

The frequency dependence of electrical transmission was investigated in six pairs by injecting into one cell a current waveform with defined spectral content (Figure 1E; Experimental Procedures). All pairs displayed typical low-pass filtering properties, with increasing attenuation and phase lag toward high frequencies (Figure 1F). As a consequence, the marked afterhyperpolarization (AHP, −66.9 ± 3.9 mV, n = 25) was transmitted through gap junctions more efficiently than the spike depolarization (spike half-width = 0.35 ± 0.09 ms, n = 25). This resulted in a biphasic postjunctional spikelet (Figure 1G), with a short initial depolarization (depolarizing junctional potential, DJP; 0.4−1.2 mV at resting potential, n = 6), followed by a prolonged hyperpolarization (hyperpolarizing junctional potential, HJP; 0.7−1.3 mV at resting potential, n = 6) (Figure 1G). The DJP and HJP peaked 0.8 ± 0.3 ms and 22.9 ± 4.8 ms, respectively, after the prejunctional spike (n = 6). Their time course was approximately predicted by a Bode-plot-based filtering of the prejunctional voltage trace (Figure S4; Experimental Procedures) (Gibson et al., 2005). Slight residual differences in the DJP time course and HJP amplitude might be explained by active amplification of the spike coupling (Figure 4) or distortion of the spike time course by the recording electrode (Gibson et al., 2005). In the voltage-clamp mode, the junctional current underlying the spikelet was also biphasic (Figure 1G), with a late outward component (HJC, 2−20 pA at −75 mV, n = 14) carrying on average 14 ± 7 (n = 14) times more charge than the initial inward component (DJC, 2−10 pA at −75 mV, n = 14) (Figure 1H). Thus, in Golgi cells, as in other interneurons displaying large AHPs (Bennett and Zukin, 2004; Galarreta and Hestrin, 2001a), the transmission of action potentials through electrical synapses results in a net hyperpolarizing effect.

Depolarization of the Golgi Cell Network Induces Gap Junction-Mediated Subthreshold Membrane Potential Oscillations in Individual Golgi Cells

The influence of electrical coupling on the temporal organization of the Golgi cell network was explored. Almost all recorded cells were silent, both in the cell-attached (n = 44/44) and whole-cell (n = 122/136) configuration, with a resting potential of −66.0 ± 5.5 mV (n = 122). In situ, Golgi cells receive excitatory synaptic inputs from parallel fibers and from mossy fibers (Dieudonne, 1998; Kanichay and Silver, 2008). Parallel fiber inputs display long-lasting kainate (KA) components (Bureau et al., 2000) that may summate during physiological regimes of activity (Chadderton et al., 2004; Jorntell and Ekerot, 2006). Selective activation of these KA receptors by bath-applied KA (0.3 or 1.0 μm) depolarized all Golgi cells, and 72% of them were driven beyond threshold (n = 27/34 whole-cell and n = 29/44 cell-attached recordings). In whole-cell recordings, the depolarization was accompanied by robust subthreshold oscillations (STOs) of the membrane potential (Figure 2A).

STOs were observed in the presence of blockers of synaptic transmission (NBQX, D-APV, SR 95531, and strychnine, n = 23) and persisted upon repolarization of the cell near resting potential (Figures 2B and 2C). At −60 mV, their amplitude averaged 2.1 ± 0.9 mV (n = 50) and was not different (p = 0.43) for the two concentrations of KA tested. A large peak in the membrane potential power spectrum (Figures 2B and 2C) indicated a clear preferred (modal) frequency of STOs. The average modal frequency for 0.3 μm KA (10.2 ± 2.5 Hz, n = 23) was significantly lower ($p < 10^{-5}$) than for 1.0 μm KA (19.0 ± 6.4 Hz, n = 26) (Figure 2D). This frequency shift mirrored the one in the firing rate of cells recorded in the cell-attached configuration: from 12.7 ± 4.9 Hz (0.3 μM KA, n = 15) to 24.4 ± 5.1 Hz (1.0 μm KA, n = 14) ($p < 10^{-4}$). STOs appeared to constrain the timing of spikes. The spike-triggered average of the subthreshold membrane potential in cells with low firing rates displayed regularly spaced side peaks, showing that spikes occurred preferentially on the depolarizing phase of STOs (Figure 2E).

STOs do not result from resonance induced by active conductances in single Golgi cells. When excited with depolarizing pulses in the absence of KA, Golgi cells fired with little adaptation (Figure S1C). Their firing rate increased linearly with the injected current with a slope of 14.6 ± 0.5 Hz per 100 pA (n = 7; Figure S1D and S1E) and no signs of bursting behavior (Figure S1C). Furthermore, STOs persisted in the presence of internal QX-314 (2 mM, n = 9) but were suppressed by bath-application of tetrodotoxin (TTX, 200 nM, n = 16, Figure 2F) or carbenoxolone (100 μM, n = 4, Figure S2B), indicating that they reflect the spiking activity of the Golgi cell network, as seen through electrical synaptic coupling.

STOs Reflect Oscillatory Synchronization of Golgi Cells

We analyzed the temporal relation of STOs in paired whole-cell recordings (ID: 30−120 μm, n = 6), in the presence of KA and blockers of synaptic transmission. In all pairs, the cross-correlation function (CCF; Experimental Procedures) of the cells' subthreshold membrane potential displayed a significant peak centered around zero lag (amplitude: 0.59 ± 0.16 for 0.3 μM KA, 0.49 ± 0.05 for 1.0 μM KA, n = 4 in both cases) (Figure 3B). CCFs also displayed significant side peaks in most cases (0.3 μM KA: −128.4 ± 46.5 ms and 120.7 ± 46.2 ms, n = 4; 1.0 μM KA: −48.1 ± 18.9 ms and 47.7 ± 19.4 ms, n = 3).

We then analyzed the temporal relation of Golgi cells firing under the same conditions, by computing cross-correlograms (CCs; Experimental Procedures) from the times of occurrence of spikes obtained in whole-cell (n = 7) or cell-attached (n = 8) paired recordings (ID: 28−156 μm) (Figure 3C). All CCs displayed a significant peak around zero lag. The synchronization strength (the peak area above Z score = 2) decreased significantly with increasing distance (Figure S5), in agreement with the decay of electrical coupling (Figure 1). Most CCs also displayed periodic side peaks (Figure 3C and S8). For 0.3 μM KA, these peaks were centered at −54 ± 10 ms and 60 ± 18 ms (n = 6), matching the periodicity of STOs.

When computed at high resolution, most CCs (n = 13/15) displayed two subpeaks around zero that were fitted using the sum

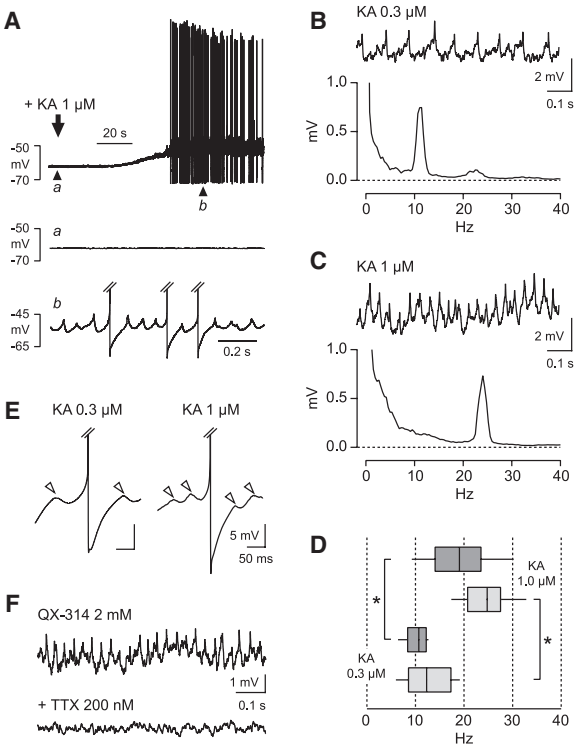

Figure 2. KA-Induced Subthreshold Oscillations of Golgi Cell Membrane Potential

(A) (Top) Response of a Golgi cell to KA application (1 μM). (Middle) Magnified view of the recording before KA application (arrow *a* in the top trace). (Bottom) Magnified view of the STO shortly after KA application (arrow *b* in the top trace).

(B and C) (Top) Steady-state STOs recorded at −60 mV in the same cell (0.3 and 1.0 μM KA, respectively). (Bottom) Corresponding power spectra.

(D) Box plots of the discharge rate (light gray) and STO modal frequency (dark gray) under KA stimulation. *$p < 10^{-4}$ (Mann-Whitney U test).

(E) Spike-triggered average membrane potential calculated in two cells with low firing rates (left: 0.3 μM KA, average of 290 spikes; right: 1.0 μM KA, average of 82 spikes). Note the regularly spaced side peaks (arrowheads).

(F) STOs recorded in the presence of 2 mM QX-314 in the pipette (top), suppressed by bath application of 200 nM TTX (bottom).

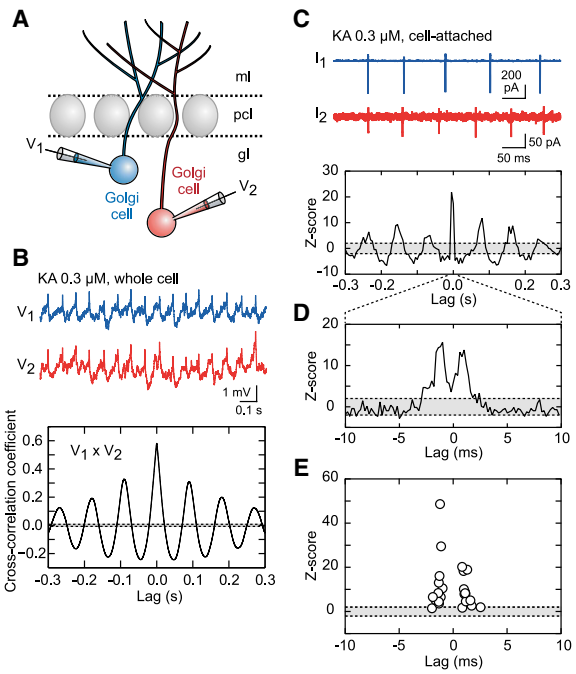

Figure 3. Synchronization of STOs and Spikes in Golgi Cell Pairs

(A) Recording configuration.

(B) KA-induced STOs (top) and their cross-correlation function (bottom) in one pair.

(C) Spike trains recorded in the cell-attached configuration during KA application (0.3 μM, top) and their cross-correlogram (CC, bin = 5 ms, bottom).

(D) Magnified view of the CC peak near zero lag, revealing two subpeaks (bin = 0.2 ms).

(E) Coordinates of the two subpeaks in 13 pairs, estimated by fitting the sum of two Gaussian curves on the CCs. In panels (B)–(E), dashed lines indicate confidence limits.

of two Gaussian curves (Figure 3D). The maxima were located on average at −1.4 ± 0.3 ms and 1.3 ± 0.5 ms (Figure 3E), with widths at half-maximum of 2.2 ± 1.2 ms and 2.6 ± 0.9 ms. The average width of the central doublet at Z score = 2 (6.2 ± 1.3 ms, n = 15, bin = 1 ms) was not significantly different in the two regimes of excitation tested (0.3 or 1.0 μM KA, p = 1.00) or in the two recording configurations (p = 0.20) and did not vary as a function of the ID (Figure S5). Comparable double-peaked synchronization patterns have been described in other electrically coupled neurons (Galarreta et al., 2004; Hu and Bloomfield, 2003; Long et al., 2002) and suggest that a spike in one cell can trigger a spike in a coupled cell within milliseconds.

The Two Components of Spikelets Have Opposite Effects on Spike Synchronization in Golgi Cell Pairs

The above results show that the activity of neighboring Golgi cells does not only display low-frequency oscillatory synchronization but also millisecond-scale spike synchronization. Spikelets produce an excitatory-inhibitory sequence in postjunctional cells, composed of a short DJP and a prolonged HJP (Figure 1G). To dissect the influences of DJPs and HJPs on the firing of Golgi cells, we examined the discharge pattern of electrically connected pairs in the absence of KA. Tonic spiking was induced in pairs of cells (ID: 28−120 μm, G_J: 0.33−1.54 nS, n = 9) by injection of steady depolarizing current (Figure 4A). The temporal organization of firing in these pairs was similar to that induced by KA applications (Figures 3C–3E). All CCs (n = 9) displayed a significant peak around zero lag, with an average width of 6.8 ± 2.6 ms at Z score = 2 (bin = 1 ms). As in the presence of KA, the synchronization strength decreased significantly with increasing distance (Figure S5). Most CCs (n = 8/9) also displayed two peaks around zero (Figure 4B), centered at −1.2 ± 0.3 ms and 1.1 ± 0.3 ms (Figure 4C), with widths at half-maximum of 2.6 ± 2.3 ms and 2.3 ± 2.0 ms. This delay between prejunctional and postjunctional spikes matches the time-to-peak of DJPs recorded in the same conditions (Figure 1G).

To further dissect the mechanism by which DJPs might trigger postjunctional spikes, the amplitude of DJPs (V_{DJP}) was measured as a function of the postjunctional membrane potential in five pairs (Figure 4D_1). In these pairs, spikes in one cell

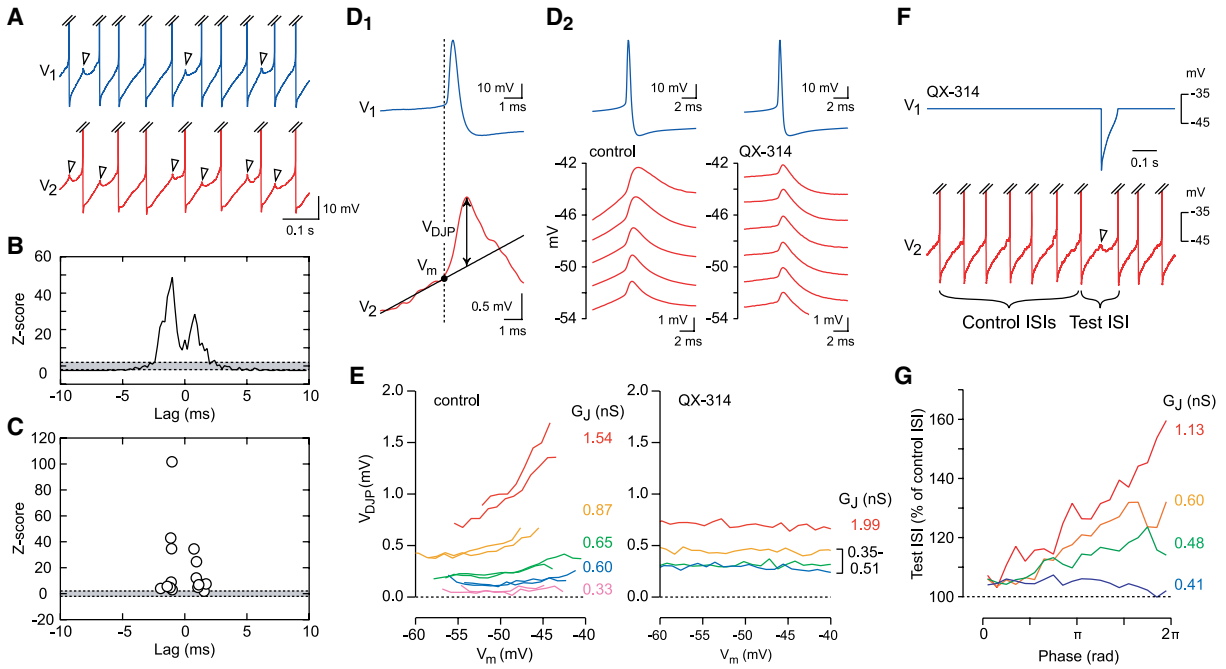

Figure 4. Spikelets Have a Dual Excitatory-Inhibitory Influence

(A) Firing pattern of a strongly coupled pair (G_J = 1.54 nS) excited by steady current injection. Arrowheads indicate spikelets produced by asynchronous spikes.

(B) Corresponding CC, displaying a double-peaked structure.

(C) Coordinates of the two subpeaks in eight pairs.

(D_1) Magnified view of a spike in cell 1 (blue) and the corresponding DJP in cell 2 (red). The membrane potential at the foot of the DJP (V_m) was measured 0.5 ms before the spike peak (dashed line). The DJP amplitude (V_{DJP}) was measured relative to a linear extrapolation of the baseline (black line). (D_2) DJPs were sorted according to V_m and averaged (bin = 2 mV) in control conditions (left) and in the presence of 2 mM internal QX-314 (right).

(E) (Left) Voltage dependence of V_{DJP} in control conditions (n = 5 pairs, each corresponding to one color). Exponential fits ($a + b.\exp[V_{DJP}/c]$) returned: a = 0.2 ± 0.2 mV, b = 2.8 ± 6.7, and c = 8.1 ± 3.7 mV (n = 10). (Right) Same relation with QX-314 in cell 2.

(F) Influence of the AHP on spike timing in coupled cells. A voltage command reproducing the AHP time course was injected into cell 1 (recorded with QX-314). The evoked HJP in cell 2 (arrow) changed the cell's firing by prolonging the ISI (compare the test ISI to control ISIs).

(G) Average phase-response curves showing the duration of the test ISI (percentage of average control ISI) plotted against the phase at which the HJP was evoked within the discharge cycle of cell 2 (bin = 18°, n = 4 pairs).

triggered spikelets at various positions in the interspike interval (ISI) of the other cell (Figure 4A). Thus, V_{DJP} could be examined across a broad range of subthreshold membrane potentials. V_{DJP} displayed a significant voltage-dependent amplification (Figures $4D_2$ and 4E). The amplification was absent when sodium channels were blocked in the postjunctional cell by adding QX-314 (2 mM) to the internal solution (n = 4; Figure 4E), indicating that voltage-dependent sodium conductances are fully responsible for the potentiation of the DJP. Active boosting of DJPs has been shown to enhance the probability to trigger a spike in the postjunctional cell (Curti and Pereda, 2004; Mann-Metzer and Yarom, 1999).

We tested whether the HJP can have an influence on firing at longer timescales. In this experiment, HJPs were evoked at random phases within the discharge cycle of one cell by repeatedly injecting the waveform of an AHP into a coupled cell (ID: 34–54 μm, G_J: 0.41–1.13 nS, n = 4; Figure 4F; Supplemental Data). The calculated phase-response curves showed that HJPs prolonged the duration of interspike intervals (Figure 4G). Furthermore, the later the HJP within the discharge cycle, the bigger the change in the ISI duration, with a linear correlation slope that strongly depended on the coupling strength (Figure 4G). This shows that the HJP can effectively delay spike firing and shape Golgi cell synchrony on longer timescales than the DJP.

Together, these results confirm that spikelets have a dual effect: excitation mediated by the DJP effectively synchronizes spikes with millisecond precision, and inhibition mediated by the HJP shifts the phase of the cells. However, experimental approaches are limited in their capacity to unravel the contribution of these two effects or other parameters to the generation of network oscillations. For this purpose, we designed a network model that incorporates all features described above.

A Golgi Cell Network Model Displays Oscillatory Behavior Similar to Experiments

Previous models have shown that electrical coupling can synchronize periodic spike emission both in single pairs (Chow and Kopell, 2000) and large neuronal networks (Pfeuty et al., 2003). These models contained few heterogeneities and modeled cells discharged in high synchrony at each cycle of the oscillation. In contrast, we report here that during KA-induced oscillations, Golgi cells have different firing rates

(Figure 2D) and can skip several cycles of subthreshold potential oscillation (Figure 2A). Hence we tested whether electrical coupling alone was sufficient to create this loosely entrained oscillatory regime, when both strong heterogeneities and realistic spatial coupling are taken into account. We modeled the Golgi cell network as a 2D array of 144 neurons (Figure 5A), reproducing experimental parameters such as the cell density (Figure S6, Supplemental Data) and the relation between G_J and ID (Figures 5B and 1D; Experimental Procedures). Golgi cells were modeled as single-compartment exponential integrate-and-fire neurons with a simplified spike-generating current and an additional AHP conductance. The spike-generating current produced both a DJP amplification and spike threshold similar to the experimental ones (data not shown). The parameters of the AHP reproduced the decay of the AHP recorded experimentally (data not shown). To mimic KA-mediated stimulation, we added an excitatory tonic conductance, drawn randomly and independently for each cell (using a Gaussian distribution of mean 1.2 nS and SD 0.36 nS) in order to introduce heterogeneity in the cells' firing rates. Upon addition of these conductances, the network became active as shown in Figure 5 (see also Movie S1). Individual firing rates varied between 0 and 21 Hz (average = 7 Hz; Figure S7B). Removal of all gap junctions in the network increased the average frequency to about 10 Hz (Figure S7B), indicating that, overall, HJPs inhibited the average firing rate in the network. The autocorrelograms of single cell spike trains displayed rhythmicity comparable to that observed in real cells (Figure S8). CCs between the spike trains of different cells also displayed rhythmicity (Figure S8). These CCs reproduced the double-peaked structure seen experimentally, with peaks at similar locations ±1 ms, though the peaks were in average smaller than the experimental ones (Figure S7B). The intracellular potential of the model cells displayed STOs that were phase locked to a 12 Hz oscillation of the overall population activity (Figures 5C–5E). Cells in the network were synchronized over several cycles as in experimental data (Figure 5F versus Figure 3B). Due to the limited spread of electrical connectivity, oscillations were loosely coherent in space, as shown by the decay of the amplitude of cross-correlations between cells as a function of their distance (Figure S8). To further investigate the mechanisms underlying this oscillation, we modified the gap junctions in model cells so that the junctional current in the postjunctional cell was only present for certain ranges of membrane potential of the prejunctional cell (Traub et al., 2001). The autocorrelation of the population activity under these different conditions is shown in Figure 5F. With standard gap junctions, the autocorrelogram was strongly oscillatory. For gap junctions that only opened when the prejunctional cell was above −35 mV, resulting in a pure excitatory effect of spikelets, the oscillation disappeared entirely, and the population activity autocorrelogram became flat (Figure 5F). When gap junctions were modified so that they were only open below −35 mV, resulting in a pure inhibitory effect of spikelets, the STO remained and the population activity autocorrelation was only slightly reduced (by roughly 35%) (Figure 5F). These results show that HJPs are a necessary component of network oscillations. On the other hand, DJPs are not necessary, in contrast with other models (Traub et al., 2001), but slightly amplify the oscillation.

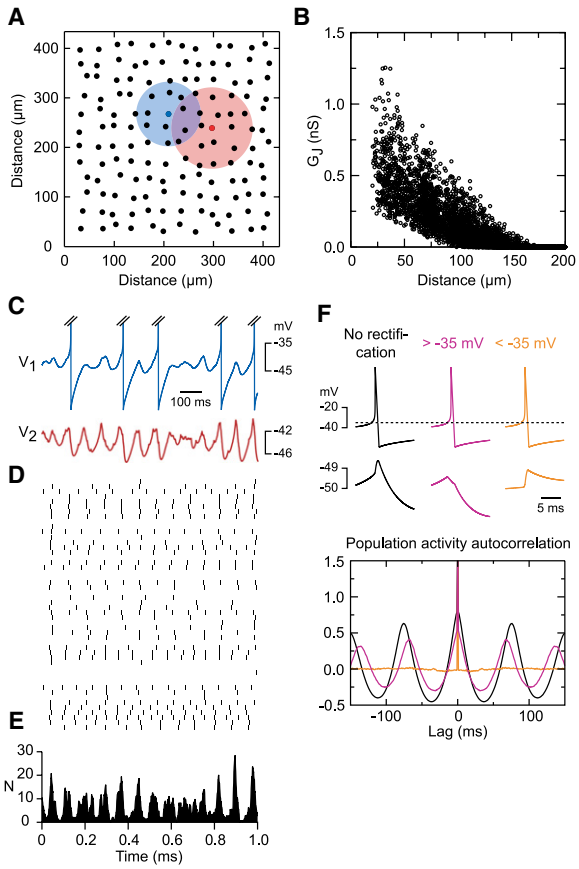

Figure 5. Design and Behavior of the 2D Golgi Cell Network Model

(A) Plot showing the position of all 144 neurons in the model (black dots). The extensions of two cells are represented by a blue and a red disk.

(B) Variation of G_J with the distance between cells.

(C–E) Membrane potential of two cells (C), raster plot (D) and population activity histogram (E) during a 1 s episode of activity. We selected one cell (red) that did not spike during this episode to better show the STO.

(F) (Top) Average spike and spikelet in a pair of cells in control conditions. The spikelet was obtained with normal (black) or rectifying (purple and orange) gap junctions. The rectification allowed us to simulate fully hyperpolarizing (purple) or depolarizing (orange) spikelets. (Bottom) Autocorrelation function of the population activity calculated on a 100 s episode, with normal (black) or rectifying (purple and orange) gap junctions. Note the abolition of the oscillatory behavior when spikelets are fully depolarizing (orange).

Electrical Coupling Allows for Low-Frequency Resonance in the Golgi Cell Network Model

In rats and monkeys, low-frequency oscillations recorded in the granular layer (GL) of hemispheric lobules are phase locked with oscillations in the sensorimotor cortex (Courtemanche and Lamarre, 2005; O'Connor et al., 2002). We tested the ability of the modeled network to respond to modulated inputs by adding a sinusoidal component to the simulated KA conductance (Experimental Procedures). The network response, measured as the modulation of the population activity at the input frequency (Figures 6A and 6B), displayed a marked resonance at its "natural" frequency (i.e., its oscillating frequency for a non-modulated drive of equivalent mean amplitude) (Figure 6C). This

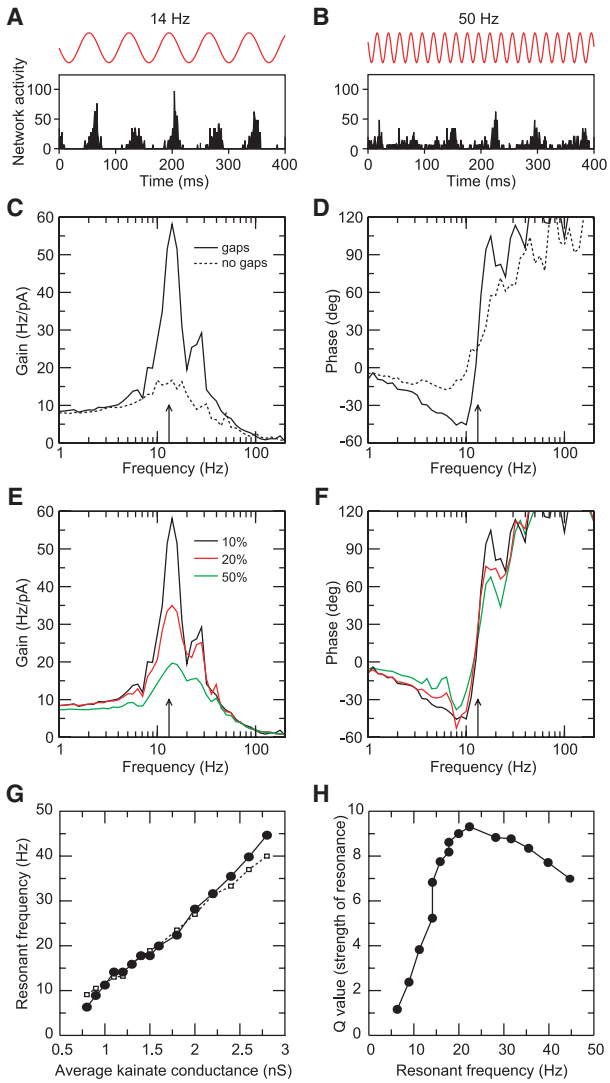

Figure 6. Tunable Resonance in the Golgi Cell Network Model

(A and B) Two oscillatory drives (red) and the associated population activity histograms (back, bin = 1 ms).

(C) Plot of the gain of the network as a function of the drive frequency for a 10% amplitude modulation of the input current. Black line, normal gap junctions; dashed line, no gap junctions. The natural oscillatory frequency of the network (see definition in the text) is indicated by the arrow in this and subsequent panels.

(D) Plot of the phase lag between the drive and the population activity modulation at the drive frequency. Black line, normal gap junctions; dashed line, no gap junctions.

(E) Plot of the gain as a function of the drive frequency for different amplitude modulations of the input current.

(F) Phase lag between the drive and the population activity modulation at the drive frequency for different amplitude modulations of the input current.

(G) The natural oscillation frequency (filled symbols) and the network resonant frequency (open symbols) are plotted against the average drive on the circuit.

(H) Strength of resonance (Q value) plotted against the network resonance frequency.

resonance was almost fully abolished when gap junctions were suppressed (Figure 6C). Interestingly, the amplification of the population activity at resonance was more pronounced for weakly modulated inputs (Figure 6E) and showed a phase lag of about 20° at the peak of the resonance for all modulation strengths. The network response could also display a phase advance (up to 45°) for driving frequencies below the resonance frequency (RF) (Figures 6D and 6F). We investigated how these resonant properties depend on the mean drive to the system by varying systematically the mean KA conductance between 0.8 and 2.4 nS, thus increasing the average firing rate of the cells and the network oscillation frequency. The RF of the network increased approximately linearly with the mean KA conductance (Figure 6G). However, the magnitude of the resonance, as measured by the Q value (ratio of modulation at RF/modulation at low frequency) was strongly dependent on the mean KA conductance. Resonance was virtually absent below 5 Hz and was maximal for a drive leading to network oscillations at 20 Hz. These results strongly suggest that the Golgi cell network can stabilize oscillatory interactions between the cerebellar cortex and other brain regions in the 5–30 Hz range, even if the incoming activity is weakly modulated.

Oscillatory Golgi Cell Activity Imposes Inhibition and Disinhibition Cycles over Granule Cells

Each Golgi cell contacts a fraction of the granule cells (Dugue et al., 2005) whereas each granule cell is contacted by several Golgi cells (Rossi and Hamann, 1998). To investigate whether oscillations in the Golgi cell network translate into modulated inhibition in granule cells, we performed Golgi cell-granule cell paired recordings (ID < 150 μm). The basal frequency of spontaneous inhibitory postsynaptic currents (IPSCs) in granule cells was low (0.30 ± 0.22 Hz, n = 7; Figure 7B). In 82% of the pairs (n = 9/11), Golgi cell spikes, triggered by brief current pulses, did not evoke IPSCs in the granule cell (Figure 7C). As expected, the frequency of IPSCs in granule cells increased ($p < 0.02$, sign test) after KA (0.3 μM) application (Figure 7B), to reach 11.05 ± 4.18 Hz (n = 7), and depressed to 0.39 ± 0.35 Hz (n = 3) after further TTX application (200 nM). KA-evoked IPSCs were locked to Golgi cell spikes, regardless of the existence of a synaptic connection. The granule cell average current triggered on Golgi cell spikes displayed a significant peak in eight out of nine pairs with no synaptic connection and significant side peaks in five of them (Figure 7C). In some recordings (n = 5), the Golgi cell was hyperpolarized to isolate the STO and assess its correlation with the IPSCs. When triggered on IPSCs half-rise, the average subthreshold membrane potential in the Golgi cell displayed significant peaks and side peaks in three out of the four pairs in which IPSCs were satisfactorily separated from the noise (Figure 7C). The absence of lag indicates that IPSCs preferentially occur on the depolarizing phase of the STO (Figure 7C). In addition, Golgi cell STOs and granule cell currents were significantly correlated (Figure 7D), with an average peak correlation of 0.14 ± 0.08 (at −9.6 ± 4.9 ms, n = 5), and significant side peaks (at −88.6 ± 38.4 ms and 62.3 ± 37.8 ms, n = 5). This indicates that maximum disinhibition of granule cells occurs slightly before the peak of the STO, while maximum inhibition develops slightly after the peak.

To confirm the synchronization of inhibition in granule cell populations, we recorded from pairs of granule cells in the presence of KA (Figure 7E). The CCF of the current traces in the two cells

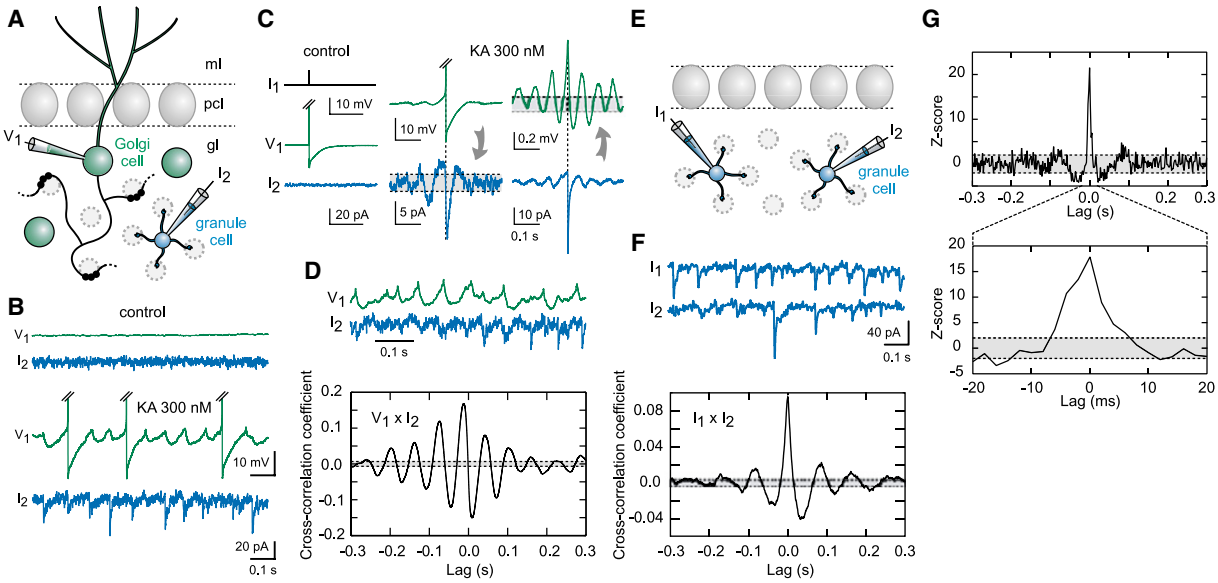

Figure 7. Golgi Cells Deliver a Coherent Rhythmic Input to Granule Cells during KA Stimulation

(A) Recording configuration. In the granular layer (gl), the axon of each Golgi cell (dark line) innervates a subset of glomeruli (gray dotted circles) in which it makes en passant varicose contacts (black dots) with granule cell dendrites (schematized around the granule cell soma). All recordings shown from (B) to (D) are from the same pair.

(B) Golgi cell membrane potential (green) and granule cell current (blue) before (top) and during (bottom) KA application (0.3 μM).

(C) (Left) Golgi cell average spike (green) and corresponding spike-triggered average current in the granule cell (blue) in basal conditions (averages of 20 sweeps). Spikes were triggered in the Golgi cell with brief pulses (800 pA, 1 ms, black). (Middle) Same calculation performed with KA-evoked spikes. (Right) Average Golgi cell subthreshold potential triggered on the half-rise of detected granule cell IPSCs.

(D) (Top) Golgi cell STO (green) recorded at −60 mV and granule cell membrane current (blue). Vertical scales are the same as in (C). (Bottom) CCF of the Golgi cell STO and granule cell current.

(E) Configuration of granule cell paired recordings.

(F) (Top) KA-induced inhibitory activity in one granule cell pair. (Bottom) CCF of the current measured in the two cells.

(G) (Top) CC of detected IPSCs in one granule cell pair. (Bottom) Expanded view of the central peak of the CC.

In all panels, dashed lines indicate the confidence limits.

(n = 6) always displayed a peak at zero lag (0.10 ± 0.05) (Figure 7F) and significant side peaks denoting a periodicity of 14.8 ± 4.2 Hz. This correlation could either result from coherent Golgi cell network activity or from the activity of Golgi cells contacting both granule cells. In the latter case, the jitter of release at independent terminals of the same Golgi cell axon should fully account for the lag between synchronous IPSCs. We showed previously that this jitter is 0.5 ± 0.12 ms (FWHM of the CC of IPSCs) (Dugue et al., 2005). Here, the CC of IPSCs, calculated in five pairs with good signal-to-noise ratio (Figure 7G) displayed on average a 2.8 times wider central peak (FWHM = 1.4 ± 0.9 ms). This distribution (full width at Z score = 2 of 3.4 ± 2.0 ms, n = 5) is similar to that of CCs calculated from spike trains of coupled Golgi cells (6.2 ± 1.3 ms, n = 15). Thus, oscillatory synchronization of the network of Golgi cells creates periods of inhibition followed by alternating periods of disinhibition in granule cells.

Golgi Cells Discharge in Phase with Low-Frequency Oscillations of the LFP during Quiet Waking In Vivo

The phasic inhibitory control of granule cells described in Figure 7 is well suited to underlie low-frequency oscillations recorded from the GL in vivo, during which intense multiunit activity, putatively arising from granule cells, occurs in phase with the LFP (Hartmann and Bower, 1998; Pellerin and Lamarre, 1997). Golgi cell firing and LFP were recorded simultaneously from the GL of unrestrained rats (Figure 8; Supplemental Data). Putative Golgi cells (n = 9) were identified using established criteria: a mean firing rate under 30 Hz (7.53 ± 4.28 Hz) and a median ISI of 40−140 ms (Holtzman et al., 2006; Vos et al., 1999). The rats were trained to keep quiet and immobile, but attentive to the environment, to maximize the occurrence of bouts of oscillations. All LFPs showed a peak in their power spectra at 6−9 Hz (6.97 ± 0.49 Hz, n = 9) (Figures 8A and 8B). Low-frequency LFP oscillations were not distributed evenly in time but presented spontaneous waxing and waning (Figure 8A). Periods of strong 6−9 Hz oscillations were selected by spectral analysis (Figure 8A and 8B). Autocorrelograms of Golgi cell spikes during these periods revealed a mild rhythmic behavior around the oscillation frequency (Figure 8C). The phase distribution of Golgi cell spikes in the LFP oscillation cycle was fitted with a Von Mises distribution and showed a significant modulation ($p < 0.05$, n = 9/9) (Figure 8E) with a preferred phase for the group at −46° ± 75°. In most cells (seven out of nine) the preferred phase was not significantly different from zero (Figure S9). Two other cells showed a marked phase advance, as expected in our model given their higher firing rate (Figure S9). Overall, the

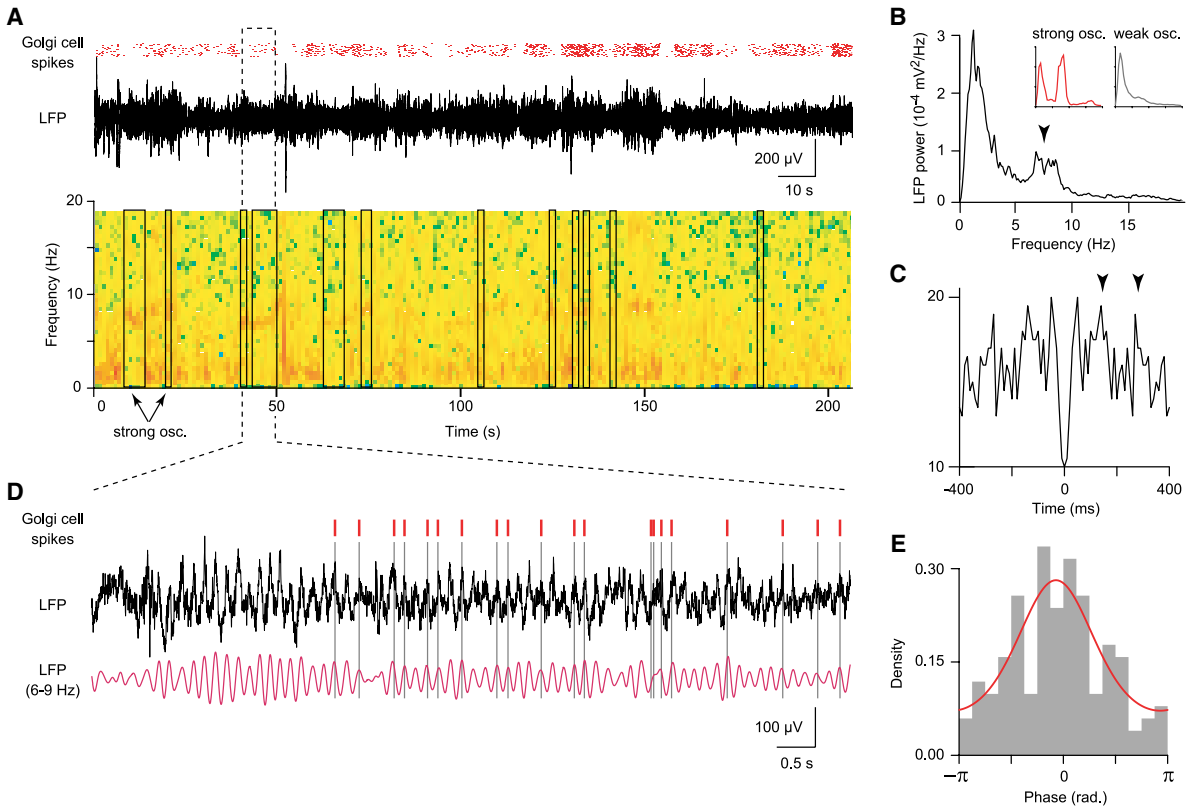

Figure 8. Golgi Cells Fire in Phase with Slow Oscillations of the Local Field Potential In Vivo

(A) Simultaneous recordings of the LFP and of putative Golgi cell units were obtained in the rat during quiet attentive waking. (Upper trace) Raster plot of the Golgi cell discharge. (Middle trace) Raw LFP (1–475 Hz). Negativities are displayed as upward deflections. (Lower panel) Spectrogram of the LFP (1 Hz to 1 kHz, sampling rate 2 kHz) for 2 s windows overlapping over 1 s. Periods of intense spectral power in the 6–9 Hz band, relative to the power in a wider 3–20 Hz band, are boxed.

(B) Power spectra of the LFP during the whole recording session and during periods of high and low oscillations, showing the efficacy of the selection procedure.

(C) Autocorrelogram of the Golgi cell discharge showing that resonance at the frequency of the LFP oscillations is present but not marked.

(D) A period of strong oscillation is represented at a larger timescale. (Lower trace) The LFP was filtered at 5–9 Hz to better illustrate the phase relationship with Golgi cell firing.

(E) Phase distribution of Golgi cell spikes relative to the negative peak of the oscillations (upward). The red line represents the best fit by a von Mises circular distribution function.

involvement of Golgi cells in low-frequency GL oscillations in vivo paralleled the oscillatory behavior of the Golgi cell network in vitro.

DISCUSSION

Electrical Coupling between Golgi Cells Is the Substrate for Low-Frequency Oscillations in the Cerebellar Granular Layer

We found that electrical interactions are a prominent feature of cerebellar Golgi cells (Figure 1) and coordinate their activity. KA induced synchronized Golgi cell firing and 5–30 Hz STOs independently of chemical transmission (Figure 2 and 3). STOs were suppressed by bath-applied but not internal sodium channel blockers (Figure 2), showing that they do not require intrinsic subthreshold oscillatory mechanisms but rely solely on network activity. Combining paired recordings and network simulations, we identified the mechanisms underlying low-frequency synchronization. Electrical transmission of the spike depolarization mediated millisecond spike synchronization as previously shown (Galarreta and Hestrin, 1999; Gibson et al., 1999), but was not sufficient to recruit Golgi cells into a common oscillatory dynamics (Figure 5). Electrical transmission of the AHP, favored by the low-pass filter properties of gap junctions, greatly influenced spike timing on longer timescales (Figure 4) and was required to obtain low-frequency population oscillations (Figure 5). In the neocortex, it has been proposed that AHP coupling sharpens the temporal window for the detection of synchronous excitatory inputs by coupled interneurons (Galarreta and Hestrin, 2001b). Here, we show that it is sufficient to generate both STOs and network oscillations (Figure 5).

Distinctive Properties of Low-Frequency Oscillations of the Golgi Cell Network

Gap-junctions are important components of rhythmogenic circuits. Both modeling and experimental studies have shown

that electrical synapses can enhance synaptically driven gamma (30–80 Hz) oscillations in hippocampal and neocortical networks (Deans et al., 2001; Kopell and Ermentrout, 2004; Traub et al., 2001). In the inferior olive, electrical synapses are involved in the emergence of a 10 Hz coherent network oscillation by coupling neurons with intrinsic subthreshold oscillatory properties (De Zeeuw et al., 2003; Khosrovani et al., 2007; Leznik and Llinas, 2005; Long et al., 2002; Placantonakis et al., 2006). In thalamic and neocortical networks, they participate in the generation of oscillatory activity by synchronizing rhythmic bursting (Beierlein et al., 2000; Fuentealba and Steriade, 2005; Hughes and Crunelli, 2007; Long et al., 2004). In contrast to these results, we show here that neither chemical transmission nor resonance properties are strictly required for the genesis of oscillations in an electrically coupled network, as suggested by theoretical studies (Lewis and Rinzel, 2000; Pfeuty et al., 2003).

The Golgi cell network model proposed here reproduces most features of Golgi cell synchronization measured experimentally (Figures 5 and S7). Theoretical studies have shown that electrical coupling generally promotes synchrony between neurons (Chow and Kopell, 2000; Lewis and Rinzel, 2003; Mancilla et al., 2007; Pfeuty et al., 2003, 2005). However, these studies have considered either pairs of cells or networks with no or weak heterogeneities, and no spatial structure. Using a realistic spatial connectivity profile, we show that oscillatory synchrony occurs in the presence of strong heterogeneities (wide firing rate and junctional conductance distributions).

The hyperpolarizing effect of AHP transmission through gap junctions may appear similar to the one of chemical synaptic inhibition, which can synchronize ensembles of sparsely connected inhibitory neurons (Brunel and Hakim, 1999; de Solages et al., 2008; Maex and De Schutter, 2003; Van Vreeswijk et al., 1994; Wang and Buzsaki, 1996). However, these mechanisms differ in several ways. First, AHP coupling through gap junctions is performed at constant membrane conductance, preserving the integrative capacity of the cell and the temporal precision of information processing, as required for proper motor control (Mauk et al., 2000). Second, junctional currents tend to equalize the membrane potential of coupled cells, speeding up the depolarization of slow-firing neurons and slowing down the depolarization of fast-firing ones. Neurons with heterogeneous levels of excitability are synchronized efficiently, as already proposed in the case of shunting inhibition (Vida et al., 2006). Finally, the kinetics of hyperpolarizing currents mediated by AHP coupling is not predetermined but follows the AHP time course, the slow part of which depends on the drive imposed on the cells. Hence, whereas inhibitory chemical synapses promote oscillations at preferred frequencies imposed by synaptic time constants and connectivity (Brunel and Hakim, 1999; Brunel and Wang, 2003), the oscillations described here may be more flexible, as their frequency adapts linearly to the drive intensity (Figure 6).

Influence of Golgi Cell Oscillatory Synchronization on Granular Layer Processing

The oscillation of Golgi cell populations may affect processing in the GL in various ways. Our model predicts that Golgi cell population activity resonates powerfully with low-amplitude drive modulations in the 5–30 Hz range, suggesting that Golgi cells can lock efficiently onto rhythmic input patterns, even when buried within a stochastic background activity. Because Golgi cells receive direct inputs from mossy fibers (Kanichay and Silver, 2008), this resonance may explain cortico-cerebellar coherence during posture maintenance and motor preparation (Courtemanche and Lamarre, 2005). Oscillations would bring Golgi cells close to threshold in phase with the occurrence of mossy fiber inputs, limiting the shunting of excitatory inputs by AHPs. In addition, oscillatory synchronization of Golgi cells would disinhibit granule cells at the onset of the mossy fiber input, enhancing granule cell excitability. This may be amplified by the resonance of granule cell intrinsic excitability at low frequencies (D'Angelo et al., 2001). Overall, 5–30 Hz oscillations of the Golgi cell network would optimize the responsiveness of the GL during tonic muscular contraction, when motor outputs and sensory inputs are sparse.

Golgi cells receive excitatory inputs from parallel fibers. A previous theoretical study has proposed that the Golgi cell-granule cell feedback circuit has a natural tendency to oscillate when granule cells fire at relatively high rates (Maex and De Schutter, 1998). The resonance mechanism described here might enhance the oscillatory behavior of this feedback loop, particularly at low levels of granule cell activity such as those observed in vivo (Chadderton et al., 2004; Jorntell and Ekerot, 2006). Furthermore, by spreading excitation along the transverse axis, parallel fibers could recruit and synchronize distant Golgi cell assemblies. This is in agreement with in vivo recordings showing local (<150 μm) synchrony of Golgi cells along the parasagittal axis and long-range synchronization (up to 2 mm) along the transverse axis (Vos et al., 1999). On-beam synchronization would bind parallel fiber inputs converging onto Purkinje cells and may optimize computation in the molecular layer (Brunel et al., 2004). In addition, inhibitory inputs to Golgi cells from molecular layer interneurons and Lugaro cells (Dumoulin et al., 2001) could coordinate low-frequency oscillations in the granular layer with higher-frequency oscillations encountered in other layers (de Solages et al., 2008; De Zeeuw et al., 2008; Isope et al., 2002).

In agreement with previous work (Holtzman et al., 2006; Vos et al., 1999), we found that Golgi cell firing is less regular in vivo, when subject to noisy synaptic drive, than in vitro, when driven by tonic KA conductances (Figure 8). Despite their irregular firing, Golgi cells discharged preferentially in phase with the negativity of LFP oscillations observed during quiet waking in vivo. This would imply that Golgi cells fire mostly in phase with the mossy fiber-granule cell population, as multiunit activity is recorded during the depolarizing phase of low-frequency oscillations in the granular layer (Courtemanche et al., 2002; Hartmann and Bower, 1998). We conclude that the gap-junction-coupled Golgi cell network participates in cerebellar processing during low-frequency oscillatory motor control.

EXPERIMENTAL PROCEDURES

For more detailed explanations of procedures, see Supplemental Data.

In Vitro Patch-Clamp Recordings

Animal experimentation methods complied with French guidelines. Parasagittal cerebellar slices were prepared as explained previously (Dugue et al., 2005) from heterozygous 20–60 days GlyT2-eGFP C57/BL6 mice, in which eGFP

expression is controlled by the promoter of GlyT2, the neuronal plasma membrane glycine transporter (Zeilhofer et al., 2005). Whole-cell and cell-attached recordings were obtained at 32°C–34°C from eGFP-positive Golgi cells and from granule cells using a Heka (Lambrecht, Germany) EPC 10 double amplifier. For Golgi cell recordings the following internal solution was used (mM): 150 $KMeSO_4$, 6 NaCl, 1 $MgCl_2$, 0.03 EGTA, 10 HEPES, 4 ATP-Mg, and 0.4 GTP-Na_2, titrated to pH 7.35 with KOH. Voltages measured with this solution were corrected for junction potential by (−6 mV, measured at 32°C). For granule cell recordings the following solution was used (mM): 145 CsCl, 10 HEPES, 1 EGTA, 5 $MgCl_2$, 0.1 $CaCl_2$, 4 ATP-Na_2, and 0.4 GTP-Na_2, titrated to pH 7.35 with N-methyl-D-glucamine. For cell-attached recordings, the pipette was filled with an HEPES-buffered ACSF containing (in mM) 141 NaCl, 2.5 KCl, 1.25 NaH_2PO_4, 10 HEPES, 25 glucose, 1.6 $CaCl_2$, and 1.5 $MgCl_2$, titrated to pH 7.4 with NaOH. Recordings were performed in the presence of 2 μM NBQX, 50 μM D-APV, 5 μM SR 95531, and 600 nM strychnine in the external solution in order to block synaptic transmission, except in the solution for Golgi cell-granule cell paired recordings, in which SR 95531 and strychnine were omitted. Golgi cells were excited by bath application of KA (0.3–1.0 μM). Chemicals and drugs were obtained from Sigma (St. Louis, MO, USA) and Tocris (Ellisville, MO, USA).

Data Analysis for In Vitro Patch-Clamp Recordings

Data were analyzed with IGOR Pro (Wavemetrics, Lake Oswego, OR, USA) and MATLAB (The MathWorks, Natick, MA, USA). Cross-correlation functions (CCFs) were calculated on 300 ms time windows shifted by 150 ms across DC-filtered recordings, and averaged. CCFs were normalized so that the autocorrelations at zero lag are identically 1. Significativity was fixed at ±2 times the average SD of shuffled CCFs (calculated from five independent computations). Spikes and synaptic currents were analyzed using SpAcAn, a custom-made threshold-detection algorithm (Dugue et al., 2005, available at http://www.neuralwiki.org/). Spike cross-correlograms (CCs) were computed from 200 s episodes of steady firing. To obtain a Z score vertical scaling, CCs were corrected by subtracting the average spike count per bin of shuffled CCs (obtained by shuffling spike trains using the same ISI distribution), and divided by the average SD of shuffled CCs. Significativity was fixed at Z score = ±2. The synchronization width (width of the CC peak at Z score = 2) and strength (peak area above Z score = 2) were calculated on CC computed with a bin of 1 ms.

The junctional conductance in Golgi cell pairs was calculated using a formalism described previously (Fortier and Bagna, 2006): a current I_1 injected into cell 1 produces a voltage change V_{11} in this cell and a voltage change V_{12} in a coupled cell 2. The coupling coefficient (K_{12}) is given by V_{12}/V_{11}. When this manipulation is repeated by injecting I_2 into cell 2, the apparent junctional conductance (G_{J12}) between the two cells can be calculated as follows: $G_{J12} = V_{12}\, I_1\, I_2/(V_{11}\, V_{22}\, I_1 - V_{12}^2\, I_2)$.

The low-pass filter property of electrical synapses was assessed by injecting into cell 1 a 15 s current waveform with defined spectral content (obtained by calculating the reverse Fourier transform of 60 sinusoids with random phases). Since the injected waveform is low-pass filtered by cell 1 before reaching cell 2, we skewed the amplitude of high frequencies toward greater values. The ratio of the magnitude (gain) and phase of individual frequencies in both cells (obtained by Fourier transform) were plotted in Bode diagrams.

The nonparametric Mann-Whitney U test and the sign test (both two-tailed) were used to test for statistical differences between two independent and two related samples, respectively. Unless otherwise stated, means ± SD are given in the text and p values are calculated using the Mann-Whitney U test. Errors indicated for linear regression coefficients are ± SD.

Extracellular In Vivo Recordings

Experimental procedures conformed to institutional policies and guidelines of the Concordia University Animal Research Ethics Committee, which follows guidelines of the Canadian Council on Animal Care. Four to eight tungsten microelectrodes were implanted in cerebellar paramedian lobules and region Crus II of male Sprague-Dawley rats (400–500 g) (Supplemental Data). After a 2 day recovery period, animals were placed daily in a recording chamber (15 cm × 30 cm) for 1 hr. Local field potentials (LFPs) and single unit activity were acquired with the Neuralynx Cheetah system (Bozeman, MT, USA) while rats were in a resting state. Unit activity was sampled at 32.5 kHz and filtered at 600–6000 Hz. LFP signals were sampled at 2 kHz and filtered at 1–475 Hz. Microelectrodes were positioned to capture optimally both 5–10 Hz LFP oscillations and spikes from GL units.

Data Analysis for In Vivo Recordings

Data were analyzed offline using NeuroExplorer (Nex Technologies, Littleton, MA), custom-made MATLAB routines (The Mathworks, Natick, MA), and GNU R (R Development Core Team, 2004). LFPs were first screened to remove periods with obvious movement artifacts. Single-unit activity was cluster-cut using built-in SpikeCut routines (Neuralynx, Bozeman, MT, USA), based on the action potential waveform. Putative Golgi cells were identified using established criteria (Holtzman et al., 2006; Vos et al., 1999). Overall, nine putative Golgi cells were identified and used for cross-correlation analyses with LFPs. The phase preference of Golgi cells was assessed for periods of highest 6–9 Hz oscillation, defined by computing the spectrogram of the LFP (1 Hz to 1 kHz, sampling rate 2 kHz) for 2 s windows overlapping over 1 s. Time intervals where the 6–9 Hz spectral power (relative to 3–20 Hz) was the highest were used. Oscillation cycles were identified by the local maxima of the LFP trace filtered by a zero lag 5–9 Hz bandpass Butterworth filter (order 6). The phase of each spike was estimated from the delay with the preceding and following oscillation cycles (phase 0 corresponding to the negative peaks of the oscillation). The significance of phase preference was tested with a Rayleigh test of uniformity of circular data. The parameters of a von Mises distribution (an equivalent to the normal distribution for circular data) were estimated by maximum likelihood, providing the preferred phase and the concentration parameter (equivalent to 1/variance of the normal distribution). A confidence interval for these parameters was obtained by bootstrap from 1000 replicates.

Model

We performed a detailed quantification of GL interneurons density (Figure S6 and Supplemental Data), which yielded a value of 9515 ± 2721 Golgi cells per mm^3 of GL. The model consisted of 144 neurons arranged on a 12 × 12 grid with 33 μm spacing, matching the experimental density assuming a mean GL thickness of 95 μm. Junctional coupling values were drawn (Supplemental Data) to yield a coupling coefficient versus distance curve and an input resistance distribution which were similar to the experimental ones. Each model neuron consisted of a single compartment whose membrane potential V obeyed the equation: $C\,(dV/dt) = -I_l - I_{Na} - I_{AHP} - I_{gap} - I_{kai}$, where C = 60 pF is the total cell capacitance, $I_l = g_l\,(V - V_l)$ is a leak current with g_l = 3 nS and V_l = −60 mV, I_{Na} is a fast sodium current, I_{AHP} is a potassium current responsible for the afterhyperpolarization (AHP), I_{gap} is the current flowing through gap junctions, and I_{kai} is the current induced by KA receptor activation. The sodium current is given by $I_{Na} = -g_l\,\Delta_T \exp[(V - V_T)/\Delta_T]$ (Fourcaud-Trocme et al., 2003), with V_T = −45 mV and Δ_T = 3 mV unless otherwise specified. When the membrane potential reaches 20 mV, it is reset to −60 mV after 1 ms following a linear trajectory. The potassium current is $I_{AHP} = g_{AHP}\, z_{AHP}\,(V - V_K)$, with g_{AHP} = 4 nS and V_K = −100 mV. The gating variable z_{AHP} follows the relaxational dynamics $dz_{AHP}/dt = (1 - z_{AHP})\, x_{AHP} - z_{AHP}/\tau_{HP}$, with τ_{AHP} = 20 ms. The source variable x_{AHP} is instantaneously increased by one unit at each spike emission and then decays exponentially with a time constant of 1 ms. The current induced by gap junctions in the i^{th} cell is $I_{gap,i} = \sum_j g_{ij}(V_i - V_j)$, where g_{ij} is the gap conductance between the i^{th} and j^{th} cells, V_i and V_j are the membrane potentials of the i^{th} and j^{th} cells. Finally, the current generated upon KA application is $I_{kai} = (V - V_E).(g_{kai} + g_N)$, where V_E = 0 mV and g_{kai} is a constant conductance drawn randomly for each cell using a Gaussian distribution of mean 1.2 nS and SD 0.36 nS. In order to reproduce the low-frequency fluctuations of the cell membrane potential in the experimental data, a slowly fluctuating conductance g_N is also taken into account. The conductance g_N is described by an Ornstein-Uhlenbeck process, $\tau_N\, dg_N/dt = -g_N + \sigma_N\sqrt{(\tau_N)}\, b(t)$, where σ_N = 0.12 nS, τ_N = 1 s, and $b(t)$ is a white-noise with unit variance density. To compute the response of the network to oscillating inputs, we added a sinusoidal component to the external current, with amplitude λg_{kai} where λ was varied from 0.1 to 0.5, and frequency f. We then computed the response of the population activity to such modulation. Specifically, we fitted the response by $r.(1 + a\cos(2\pi ft - \Psi))$ where r is the average firing rate, a/λ is the gain, and Ψ is the phase lag.

SUPPLEMENTAL DATA

The Supplemental Data include Experimental Procedures, figures, and a movie and can be found with this article online at http://www.neuron.org/supplemental/S0896-6273(08)01021-0.

ACKNOWLEDGMENTS

This work was supported by ANR (05-Neur-030), CNRS, INSERM, ENS, NSERC, and NAAR. We thank H.U. Zeilhofer for providing the GlyT2-eGFP mice and B. Barbour, A. Feltz, and J. Neyton for helpful discussion on the manuscript.

Accepted: November 6, 2008
Published: January 14, 2009

REFERENCES

Albus, J. (1971). A theory of cerebellar function. Math. Biosci. *10*, 25–61.

Baker, S.N., Kilner, J.M., Pinches, E.M., and Lemon, R.N. (1999). The role of synchrony and oscillations in the motor output. Exp. Brain Res. *128*, 109–117.

Beierlein, M., Gibson, J.R., and Connors, B.W. (2000). A network of electrically coupled interneurons drives synchronized inhibition in neocortex. Nat. Neurosci. *3*, 904–910.

Belluardo, N., Mudo, G., Trovato-Salinaro, A., Le Gurun, S., Charollais, A., Serre-Beinier, V., Amato, G., Haefliger, J.A., Meda, P., and Condorelli, D.F. (2000). Expression of connexin36 in the adult and developing rat brain. Brain Res. *865*, 121–138.

Bennett, M.V., and Zukin, R.S. (2004). Electrical coupling and neuronal synchronization in the Mammalian brain. Neuron *41*, 495–511.

Blatow, M., Rozov, A., Katona, I., Hormuzdi, S.G., Meyer, A.H., Whittington, M.A., Caputi, A., and Monyer, H. (2003). A novel network of multipolar bursting interneurons generates theta frequency oscillations in neocortex. Neuron *38*, 805–817.

Brunel, N., and Hakim, V. (1999). Fast global oscillations in networks of integrate-and-fire neurons with low firing rates. Neural Comput. *11*, 1621–1671.

Brunel, N., and Wang, X.J. (2003). What determines the frequency of fast network oscillations with irregular neural discharges? I. Synaptic dynamics and excitation-inhibition balance. J. Neurophysiol. *90*, 415–430.

Brunel, N., Hakim, V., Isope, P., Nadal, J.P., and Barbour, B. (2004). Optimal information storage and the distribution of synaptic weights: perceptron versus Purkinje cell. Neuron *43*, 745–757.

Bureau, I., Dieudonne, S., Coussen, F., and Mulle, C. (2000). Kainate receptor-mediated synaptic currents in cerebellar Golgi cells are not shaped by diffusion of glutamate. Proc. Natl. Acad. Sci. USA *97*, 6838–6843.

Chadderton, P., Margrie, T.W., and Hausser, M. (2004). Integration of quanta in cerebellar granule cells during sensory processing. Nature *428*, 856–860.

Chow, C.C., and Kopell, N. (2000). Dynamics of spiking neurons with electrical coupling. Neural Comput. *12*, 1643–1678.

Condorelli, D.F., Belluardo, N., Trovato-Salinaro, A., and Mudo, G. (2000). Expression of Cx36 in mammalian neurons. Brain Res. Brain Res. Rev. *32*, 72–85.

Courtemanche, R., and Lamarre, Y. (2005). Local field potential oscillations in primate cerebellar cortex: synchronization with cerebral cortex during active and passive expectancy. J. Neurophysiol. *93*, 2039–2052.

Courtemanche, R., Pellerin, J.P., and Lamarre, Y. (2002). Local field potential oscillations in primate cerebellar cortex: modulation during active and passive expectancy. J. Neurophysiol. *88*, 771–782.

Curti, S., and Pereda, A.E. (2004). Voltage-dependent enhancement of electrical coupling by a subthreshold sodium current. J. Neurosci. *24*, 3999–4010.

D'Angelo, E., Nieus, T., Maffei, A., Armano, S., Rossi, P., Taglietti, V., Fontana, A., and Naldi, G. (2001). Theta-frequency bursting and resonance in cerebellar granule cells: experimental evidence and modeling of a slow k+-dependent mechanism. J. Neurosci. *21*, 759–770.

Davidson, J.S., Baumgarten, I.M., and Harley, E.H. (1986). Reversible inhibition of intercellular junctional communication by glycyrrhetinic acid. Biochem. Biophys. Res. Commun. *134*, 29–36.

De Schutter, E., and Bjaalie, J.G. (2001). Coding in the granular layer of the cerebellum. Prog. Brain Res. *130*, 279–296.

De Schutter, E., Vos, B., and Maex, R. (2000). The function of cerebellar Golgi cells revisited. Prog. Brain Res. *124*, 81–93.

de Solages, C., Szapiro, G., Brunel, N., Hakim, V., Isope, P., Buisseret, P., Rousseau, C., Barbour, B., and Lena, C. (2008). High-frequency organization and synchrony of activity in the purkinje cell layer of the cerebellum. Neuron *58*, 775–788.

De Zeeuw, C.I., Chorev, E., Devor, A., Manor, Y., Van Der Giessen, R.S., De Jeu, M.T., Hoogenraad, C.C., Bijman, J., Ruigrok, T.J., French, P., et al. (2003). Deformation of network connectivity in the inferior olive of connexin 36-deficient mice is compensated by morphological and electrophysiological changes at the single neuron level. J. Neurosci. *23*, 4700–4711.

De Zeeuw, C.I., Hoebeek, F.E., and Schonewille, M. (2008). Causes and consequences of oscillations in the cerebellar cortex. Neuron *58*, 655–658.

Deans, M.R., Gibson, J.R., Sellitto, C., Connors, B.W., and Paul, D.L. (2001). Synchronous activity of inhibitory networks in neocortex requires electrical synapses containing connexin36. Neuron *31*, 477–485.

Deuschl, G., and Bergman, H. (2002). Pathophysiology of nonparkinsonian tremors. Mov. Disord. *17* (*Suppl 3*), S41–S48.

Dieudonne, S. (1998). Submillisecond kinetics and low efficacy of parallel fibre-Golgi cell synaptic currents in the rat cerebellum. J. Physiol. *510*, 845–866.

Dugue, G.P., Dumoulin, A., Triller, A., and Dieudonne, S. (2005). Target-dependent use of co-released inhibitory transmitters at central synapses. J. Neurosci. *25*, 6490–6498.

Dumoulin, A., Triller, A., and Dieudonne, S. (2001). IPSC kinetics at identified GABAergic and mixed GABAergic and glycinergic synapses onto cerebellar Golgi cells. J. Neurosci. *21*, 6045–6057.

Forti, L., Cesana, E., Mapelli, J., and D'Angelo, E. (2006). Ionic mechanisms of autorhythmic firing in rat cerebellar Golgi cells. J. Physiol. *574*, 711–729.

Fortier, P.A., and Bagna, M. (2006). Estimating conductances of dual-recorded neurons within a network of coupled cells. J. Theor. Biol. *240*, 501–510.

Fourcaud-Trocme, N., Hansel, D., van Vreeswijk, C., and Brunel, N. (2003). How spike generation mechanisms determine the neuronal response to fluctuating inputs. J. Neurosci. *23*, 11628–11640.

Fuentealba, P., and Steriade, M. (2005). The reticular nucleus revisited: intrinsic and network properties of a thalamic pacemaker. Prog. Neurobiol. *75*, 125–141.

Galarreta, M., and Hestrin, S. (1999). A network of fast-spiking cells in the neocortex connected by electrical synapses. Nature *402*, 72–75.

Galarreta, M., and Hestrin, S. (2001a). Electrical synapses between GABA-releasing interneurons. Nat. Rev. Neurosci. *2*, 425–433.

Galarreta, M., and Hestrin, S. (2001b). Spike transmission and synchrony detection in networks of GABAergic interneurons. Science *292*, 2295–2299.

Galarreta, M., Erdelyi, F., Szabo, G., and Hestrin, S. (2004). Electrical coupling among irregular-spiking GABAergic interneurons expressing cannabinoid receptors. J. Neurosci. *24*, 9770–9778.

Gibson, J.R., Beierlein, M., and Connors, B.W. (1999). Two networks of electrically coupled inhibitory neurons in neocortex. Nature *402*, 75–79.

Gibson, J.R., Beierlein, M., and Connors, B.W. (2005). Functional properties of electrical synapses between inhibitory interneurons of neocortical layer 4. J. Neurophysiol. *93*, 467–480.

Gray, C.M. (1994). Synchronous oscillations in neuronal systems: mechanisms and functions. J. Comput. Neurosci. *1*, 11–38.

Hartmann, M.J., and Bower, J.M. (1998). Oscillatory activity in the cerebellar hemispheres of unrestrained rats. J. Neurophysiol. *80*, 1598–1604.

Holtzman, T., Rajapaksa, T., Mostofi, A., and Edgley, S.A. (2006). Different responses of rat cerebellar Purkinje cells and Golgi cells evoked by widespread convergent sensory inputs. J. Physiol. *574*, 491–507.

Hu, E.H., and Bloomfield, S.A. (2003). Gap junctional coupling underlies the short-latency spike synchrony of retinal alpha ganglion cells. J. Neurosci. *23*, 6768–6777.

Hughes, S.W., and Crunelli, V. (2007). Just a phase they're going through: the complex interaction of intrinsic high-threshold bursting and gap junctions in the generation of thalamic alpha and theta rhythms. Int. J. Psychophysiol. *64*, 3–17.

Isope, P., Dieudonne, S., and Barbour, B. (2002). Temporal organization of activity in the cerebellar cortex: a manifesto for synchrony. Ann. N Y Acad. Sci. *978*, 164–174.

Jorntell, H., and Ekerot, C.F. (2006). Properties of somatosensory synaptic integration in cerebellar granule cells in vivo. J. Neurosci. *26*, 11786–11797.

Kanichay, R.T., and Silver, R.A. (2008). Synaptic and cellular properties of the feedforward inhibitory circuit within the input layer of the cerebellar cortex. J. Neurosci. *28*, 8955–8967.

Khosrovani, S., Van Der Giessen, R.S., De Zeeuw, C.I., and De Jeu, M.T. (2007). In vivo mouse inferior olive neurons exhibit heterogeneous subthreshold oscillations and spiking patterns. Proc. Natl. Acad. Sci. USA *104*, 15911–15916.

Kistler, W.M., and De Zeeuw, C.I. (2003). Time windows and reverberating loops: a reverse-engineering approach to cerebellar function. Cerebellum *2*, 44–54.

Kistler, W.M., van Hemmen, J.L., and De Zeeuw, C.I. (2000). Time window control: a model for cerebellar function based on synchronization, reverberation, and time slicing. Prog. Brain Res. *124*, 275–297.

Kopell, N., and Ermentrout, B. (2004). Chemical and electrical synapses perform complementary roles in the synchronization of interneuronal networks. Proc. Natl. Acad. Sci. USA *101*, 15482–15487.

Lewis, T.J., and Rinzel, J. (2000). Self-organized synchronous oscillations in a network of excitable cells coupled by gap junctions. Network *11*, 299–320.

Lewis, T.J., and Rinzel, J. (2003). Dynamics of spiking neurons connected by both inhibitory and electrical coupling. J. Comput. Neurosci. *14*, 283–309.

Leznik, E., and Llinas, R. (2005). Role of gap junctions in synchronized neuronal oscillations in the inferior olive. J. Neurophysiol. *94*, 2447–2456.

Long, M.A., Deans, M.R., Paul, D.L., and Connors, B.W. (2002). Rhythmicity without synchrony in the electrically uncoupled inferior olive. J. Neurosci. *22*, 10898–10905.

Long, M.A., Landisman, C.E., and Connors, B.W. (2004). Small clusters of electrically coupled neurons generate synchronous rhythms in the thalamic reticular nucleus. J. Neurosci. *24*, 341–349.

Maex, R., and De Schutter, E. (1998). Synchronization of golgi and granule cell firing in a detailed network model of the cerebellar granule cell layer. J. Neurophysiol. *80*, 2521–2537.

Maex, R., and De Schutter, E. (2003). Resonant synchronization in heterogeneous networks of inhibitory neurons. J. Neurosci. *23*, 10503–10514.

Mancilla, J.G., Lewis, T.J., Pinto, D.J., Rinzel, J., and Connors, B.W. (2007). Synchronization of electrically coupled pairs of inhibitory interneurons in neocortex. J. Neurosci. *27*, 2058–2073.

Mann-Metzer, P., and Yarom, Y. (1999). Electrotonic coupling interacts with intrinsic properties to generate synchronized activity in cerebellar networks of inhibitory interneurons. J. Neurosci. *19*, 3298–3306.

Marr, D. (1969). A theory of cerebellar cortex. J. Physiol. *202*, 437–470.

Mauk, M.D., Medina, J.F., Nores, W.L., and Ohyama, T. (2000). Cerebellar function: coordination, learning or timing? Curr. Biol. *10*, R522–R525.

O'Connor, S.M., Berg, R.W., and Kleinfeld, D. (2002). Coherent electrical activity between vibrissa sensory areas of cerebellum and neocortex is enhanced during free whisking. J. Neurophysiol. *87*, 2137–2148.

Palkovits, M., Magyar, P., and Szentagothai, J. (1971). Quantitative histological analysis of the cerebellar cortex in the cat. II. Cell numbers and densities in the granular layer. Brain Res. *32*, 15–30.

Pellerin, J.P., and Lamarre, Y. (1997). Local field potential oscillations in primate cerebellar cortex during voluntary movement. J. Neurophysiol. *78*, 3502–3507.

Pfeuty, B., Mato, G., Golomb, D., and Hansel, D. (2003). Electrical synapses and synchrony: the role of intrinsic currents. J. Neurosci. *23*, 6280–6294.

Pfeuty, B., Mato, G., Golomb, D., and Hansel, D. (2005). The combined effects of inhibitory and electrical synapses in synchrony. Neural Comput. *17*, 633–670.

Placantonakis, D.G., Bukovsky, A.A., Aicher, S.A., Kiem, H.P., and Welsh, J.P. (2006). Continuous electrical oscillations emerge from a coupled network: a study of the inferior olive using lentiviral knockdown of connexin36. J. Neurosci. *26*, 5008–5016.

R Development Core Team. (2004). R: A Language and Environment for Statistical Computing (Vienna, Austria: R Foundation for Statistical Computing). http://www.R-project.org.

Ray, A., Zoidl, G., Weickert, S., Wahle, P., and Dermietzel, R. (2005). Site-specific and developmental expression of pannexin1 in the mouse nervous system. Eur. J. Neurosci. *21*, 3277–3290.

Ray, A., Zoidl, G., Wahle, P., and Dermietzel, R. (2006). Pannexin expression in the cerebellum. Cerebellum *5*, 189–192.

Rossi, D.J., and Hamann, M. (1998). Spillover-mediated transmission at inhibitory synapses promoted by high affinity alpha6 subunit GABA(A) receptors and glomerular geometry. Neuron *20*, 783–795.

Salenius, S., and Hari, R. (2003). Synchronous cortical oscillatory activity during motor action. Curr. Opin. Neurobiol. *13*, 678–684.

Salinas, E., and Sejnowski, T.J. (2001). Correlated neuronal activity and the flow of neural information. Nat. Rev. Neurosci. *2*, 539–550.

Schnitzler, A., and Gross, J. (2005). Normal and pathological oscillatory communication in the brain. Nat. Rev. Neurosci. *6*, 285–296.

Sejnowski, T.J., and Paulsen, O. (2006). Network oscillations: emerging computational principles. J. Neurosci. *26*, 1673–1676.

Simat, M., Parpan, F., and Fritschy, J.M. (2007). Heterogeneity of glycinergic and gabaergic interneurons in the granule cell layer of mouse cerebellum. J. Comp. Neurol. *500*, 71–83.

Singer, W. (1999). Neuronal synchrony: a versatile code for the definition of relations? Neuron *24*, 49–65.

Soteropoulos, D.S., and Baker, S.N. (2006). Cortico-cerebellar coherence during a precision grip task in the monkey. J. Neurophysiol. *95*, 1194–1206.

Traub, R.D., Kopell, N., Bibbig, A., Buhl, E.H., LeBeau, F.E., and Whittington, M.A. (2001). Gap junctions between interneuron dendrites can enhance synchrony of gamma oscillations in distributed networks. J. Neurosci. *21*, 9478–9486.

Van Vreeswijk, C., Abbott, L.F., and Ermentrout, G.B. (1994). When inhibition not excitation synchronizes neural firing. J. Comput. Neurosci. *1*, 313–321.

Varela, F., Lachaux, J.P., Rodriguez, E., and Martinerie, J. (2001). The brainweb: phase synchronization and large-scale integration. Nat. Rev. Neurosci. *2*, 229–239.

Vida, I., Bartos, M., and Jonas, P. (2006). Shunting inhibition improves robustness of gamma oscillations in hippocampal interneuron networks by homogenizing firing rates. Neuron *49*, 107–117.

Vogt, A., Hormuzdi, S.G., and Monyer, H. (2005). Pannexin1 and Pannexin2 expression in the developing and mature rat brain. Brain Res. Mol. Brain Res. *141*, 113–120.

Vos, B.P., Maex, R., Volny-Luraghi, A., and De Schutter, E. (1999). Parallel fibers synchronize spontaneous activity in cerebellar Golgi cells. J. Neurosci. *19*, RC6.

Wang, X.J., and Buzsaki, G. (1996). Gamma oscillation by synaptic inhibition in a hippocampal interneuronal network model. J. Neurosci. *16*, 6402–6413.

Zappala, A., Cicero, D., Serapide, M.F., Paz, C., Catania, M.V., Falchi, M., Parenti, R., Panto, M.R., La Delia, F., and Cicirata, F. (2006). Expression of pannexin1 in the CNS of adult mouse: cellular localization and effect of 4-aminopyridine-induced seizures. Neuroscience *141*, 167–178.

Zeilhofer, H.U., Studler, B., Arabadzisz, D., Schweizer, C., Ahmadi, S., Layh, B., Bosl, M.R., and Fritschy, J.M. (2005). Glycinergic neurons expressing enhanced green fluorescent protein in bacterial artificial chromosome transgenic mice. J. Comp. Neurol. *482*, 123–141.